

Analytical Minimization-Based Regularized Sub-Pixel Shear Wave Tracking for Ultrasound Elastography

Mahmoud Derakhshan Horeh, Amir Asif, Hassan Rivaz

Abstract—Ultrasound elastography is a convenient and affordable method for imaging mechanical properties of tissue, which are often correlated with pathologies. An emerging novel elastography technique applies an external acoustic radiation force (ARF) to generate shear wave in the tissue, and uses ultrasound imaging to track the shear wave. Accurate tracking of the small tissue motion is a critical step in shear wave elastography, but is challenging due to various sources of noise in the ultrasound data. We formulate tissue displacement estimation as an optimization problem and propose two computationally efficient approaches to estimate the displacement field. The first algorithm is referred to as dynamic programming analytic minimization (DPAM), which utilizes first order Taylor series expansion of the highly nonlinear cost function to allow for its efficient optimization, and was previously proposed for quasi-static elastography. The second algorithm is a novel technique that utilizes second order derivatives of the non-linear cost function. We call the new algorithm second-order analytic minimization elastography (SESAME). We compare DMAP and SESAME to the standard normalized cross correlation (NCC) approach in the context of displacement and speed estimation of wave propagation in shear wave elastography (SWE). The results of micrometer-order displacement estimation in a uniform simulation phantom illustrate that SESAME outperforms DPAM, which in turn outperforms NCC in terms of signal to noise ratio (SNR) and jitter. In addition, the relative difference between true and reconstructed shear modulus (averaged over excitations at different focal depths and several scatterer realizations at each depth) is approximately 3.41%, 1.12% and 1.01%, respectively, for NCC, DPAM and SESAME. The performance of the proposed methods is also assessed with real data acquired using a tissue-mimicking phantom, wherein, in comparison to NCC, DPAM and SESAME improve the SNR of displacement estimates by 7.6 dB and 9.5 dB, respectively. Experimental results on a tissue-mimicking phantom also show that shear modulus reconstruction substantially improved with the proposed DPAM technique over NCC, and with some further improvement achieved by utilizing the second order Taylor series approximation in SESAME instead of the first-order DPAM.

Index Terms—Shear wave elastography (SWE), Acoustic radiation force, Regularized cost function, Dynamic programming.

I. INTRODUCTION

DURING the past two decades, several ultrasound imaging techniques have been proposed to investigate the mechanical properties of the tissue [1]–[7]. These techniques are generally referred to as ultrasound elastography and can be broadly categorized into two different groups of quasi-static and dynamic elastography approaches. In quasi-static

elastography [2], [8], a slow, relatively static compression is applied to the tissue and the ultrasound Radio Frequency (RF) signals acquired before and after the compression are correlated to estimate tissue displacements. In dynamic elastography [1], [3]–[6], [9], tissue deformation occurs at a faster rate and the propagation of mechanical waves are used to derive the mechanical properties of the tissue. Although both static and dynamic approaches use ultrasound to track the displacements, the difference lies in the applied perturbation, which can be either quasi-static or time-varying. Depending on the type of excitation, dynamic elastography itself can be further categorized into several subgroups, including radiation-force-based imaging which generates a deep “push” in the tissue by utilizing a non-invasive focused acoustic radiation force (ARF) to a focal point in the tissue [1], [3]–[6], [9], [10] in order to deform tissue and subsequently track the deformation for estimating tissue elasticity E , both quantitatively and qualitatively. Mathematically, the force generated by acoustic radiation in soft tissue is expressed as

$$F = \frac{2\alpha I}{c}, \quad (1)$$

where I denotes the temporal average intensity at a given point in space, α is the absorption coefficient of the medium, and c the speed of sound. For a given region of excitation (ROE), the radiation force is uniform if all three parameters $\{I, \alpha, c\}$ are relatively constant across the ROE. Alternatively, variations in these parameters represent the inhomogeneity in the medium and can be used to derive the mechanical properties of the tissue.

Tissue response to the ARF can be monitored using the ultrasound RF data collected immediately before and after the ARF excitation. Depending on where the resulting disturbance is monitored, two imaging approaches are proposed [11]: 1) Acoustic radiation force impulse (ARFI) imaging, wherein tissue deformation is tracked within the ROE. 2) Shear wave elastography (SWE), which unlike ARFI monitors the tissue response away from the ROE to quantitatively estimate the tissue properties from the estimated shear wave speed (SWS) [3], [9], [12]. In this paper, our focus is primarily on SWE.

In SWE, a localized and focused radiation force F is applied to the ROE to induce a shear wave that travels away from the ROE within the region of interest (ROI). During the propagation phase, the displacement field and associated attenuation of the propagating wave contain useful information about the local mechanical properties of the tissue. The displacement

M.D. Horreh, A. Asif and H. Rivaz are with Electrical and Computer Engineering, Concordia University, Montreal, QC. Emails: amir.asif@concordia.ca, m_erakhs@encs.concordia.ca, hrivaz@ece.concordia.ca

field in the tissue is often tracked by high frame rate imaging by exploiting plane-wave imaging [9], [13]. By comparing frames following the excitation to the reference frame (imaged when the tissue is at rest), the tissue displacement profile or alternatively the propagation velocity of the shear wave can be determined in both spatial and temporal domains [1], [10], [11], [14]. In an elastic isotropic medium, the relationship between the shear modulus and wave propagation speed is given by the expression

$$c_T = \sqrt{\frac{\mu}{\rho}}, \quad (2)$$

where c_T , μ and ρ represent the propagation speed, tissue shear modulus and tissue density, respectively. Recently, numerous advances have been made in recovering the shear modulus from the displacement fields [1], [5], [15]–[18]. The algebraic inversion of the Helmholtz equation has been successfully applied in MR elastography [19]–[22]. However, this technique has achieved limited success in ultrasound elastography since it involves second-order derivatives and 3D displacement estimates [3], [5], [15], [23]. Therefore, estimation of the SWS is a more common approach, which entails calculating the wavefront arrival time at different lateral positions (i.e., time-of-flight (TOF)) [16], [24]–[28].

Both inversion of the Helmholtz equation and estimation of the TOF require an accurate and precise displacement estimation, which is challenging since these displacements are very small and the data is noisy. Several post processing techniques have, therefore, been proposed to limit the effect of incorrect displacement estimates [27], [29], [30] or generate confidence index in SWE [31]. The development of accurate displacement estimation techniques remains an active field of research.

The correlation-based approaches are commonly used for displacement estimation, wherein RF data is divided into small windows and displacement is estimated by maximizing cross correlation metrics [32]–[34]. These methods are computationally efficient and have been widely used for estimating displacement fields in the SWE. However, they may generate incorrect estimates mainly due to insufficient information in the correlation window and have a higher Cramer Rao lower bound (CRLB) implying more mean square error. To address these issues, references [35], [36] proposed incorporating knowledge of adjacent displacement estimates into the final estimate of a displacement. In another work, Byram *et al.* [37] proposed Bayesian speckle tracking (or Bayesian regularization) to improve the displacement field using *a priori* knowledge of the estimation, and showed that with a simple prior scheme, the CRLB can be surpassed. Dumont & Byram [38] expanded this work and proposed a Bayesian estimator that uses a generalized-Gaussian Markov Random Field (GGMRF) prior that can automatically adjust the distribution of the prior function. While this method produces high quality displacement maps, it is not immediately suitable for real-time displacement estimation due to its high computational complexity. To overcome these limitations and to further improve the accuracy of the displacement estimation,

we adopt the dynamic programming analytic minimization (DPAM) framework, originally proposed for quasi-static elastography [39], [40], in SWE. A cost function that incorporates RF data and prior information of displacement continuity is optimized to calculate the displacement field. Nonlinear terms in the cost function are linearized using their first order Taylor series approximations to allow for efficient optimization of the cost function.

The paper seeks to further improve the accuracy of the displacement field estimate over [39], [40] by incorporating a higher order Taylor series expansion into the cost function. Since inclusion of these terms makes the optimization problem intractable, we propose a novel approach to substantially reduce the computational complexity. We refer to our method as second-order analytic minimization elastography (SESAME). Incorporating second order derivatives was recently proposed in a short abstract [41] in quasi-static elastography. Both DPAM and SESAME generate high quality displacement maps in real time and are, therefore, suitable for their online implementation.

The contributions of this work are twofold. First, we extend the DPAM framework, proposed previously for quasi-static elastography, for the first time in SWE. Second, we introduce SESAME, a novel technique for tracking displacements using RF data. A short version of this paper is published recently in a conference paper [42]. This paper is organized as follows. We first describe Dynamic Programming (DP), which provides the initial step in the proposed methods. Then we outline the details of DPAM and SESAME algorithms for tracking shear wave and then describe our approach for generating simulation and experimental data in Section II. We validate the proposed algorithms in Section III, provide discussions of the results in Section IV, and conclude the paper in Section V.

II. METHODS

In SWE, a reference ultrasound frame is initially collected from the tissue. An ARF excites a small region (shown as the yellow ellipse in Fig. 1 (a)), which is followed by collecting multiple ultrasound frames as shown in Fig. 1 (b) to monitor the propagation of the shear wave. The reference frame is collected before applying the ARF, while the remaining frames are collected during the wave propagation phase.

Let $I_1(i, j)$ and $I_2(i, j)$ be two ultrasound frames prior to and during deformation as shown in Fig. 1 (c)-(d). Symbol I denotes the intensity of a discretized sample of the RF signal with $i = 1, \dots, m$ and $j = 1, \dots, n$ representing respectively the axial (z) and lateral (x) locations of the pixel. The goal of the tracking method is to find two matrices A and L such that their $(i, j)^{\text{th}}$ elements, i.e., $a(i, j) \in A$ and $l(i, j) \in L$ provide estimates of the axial and lateral displacement for pixel (i, j) . Note that the traditional window-based techniques calculate displacement for each window, whereas our goal is to estimate displacement for each pixel. Our algorithm has two main parts. In the first part, global optimization is performed using DP to estimate displacement for one “seed” RF-line. The location of the “seed” RF-line location is not a factor that impacts the results of the proposed approach. As a matter

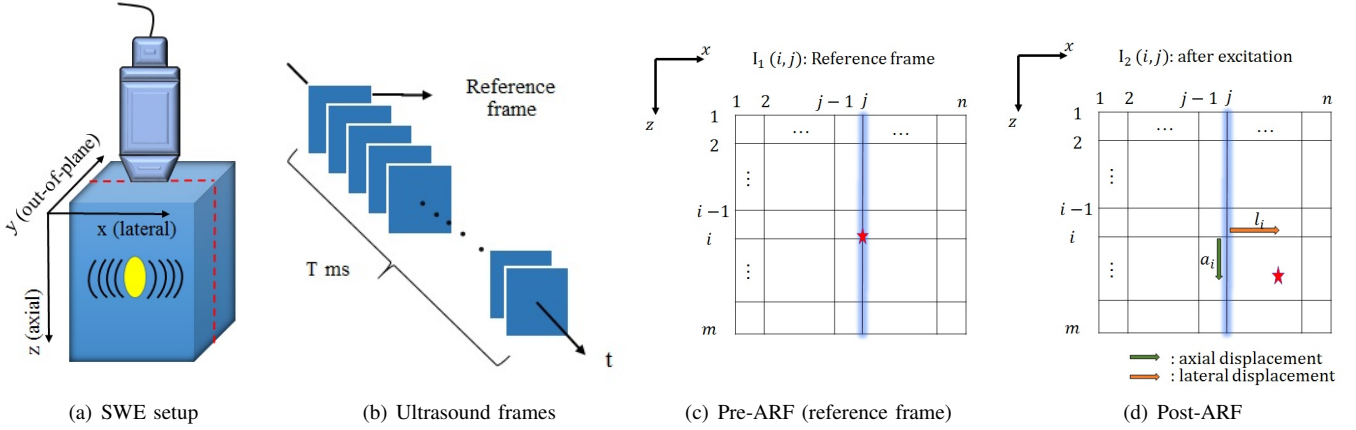


Fig. 1. Schematics of SWE. In (a), ARF generates excitation in the ROE (shown as a yellow ellipse) resulting in the propagation of shear waves from the ROE to the sides. The reference tissue is imaged at the cross section specified by red dashed lines in (a), which generates a sequence of ultrasound images shown in (b). To track the associated wave propagation, displacements for sample (i, j) (marked by a red star in (c)) in the reference frame are calculated by matching it with its corresponding point (marked by another red star in (d)).

of fact, any vertical column in the image can be used as the initial “seed” RF-line. The only limitation is that “seed” RF-line should not be chosen on the ARF focal point, which undergoes complex motions. This is an integer optimization wherein the displacement map is restricted to integer values. In the second part, a local optimization step, DPAM or SESAME, is carried out to generate sub-integer displacement maps. Since the RF data alone can be noisy and insufficient at certain locations for the estimation of the displacement field, we incorporate the prior information of the displacement field, as a regularization term. The combination of global and local optimization, as well as this regularization term, makes our algorithm robust to noise and artifacts in the RF data. Below, the DP, DPAM and SESAME approaches are introduced next.

A. Dynamic Programming (DP)

To describe the DP formulation [43], we consider a single column j (RF-line j) of the image $I_1(i, j)$ prior to excitation as highlighted with blue colour in Fig. 1 (c)-(d). For sample i , we denote the axial and lateral displacements by $\{a_i, l_i\}$. The prior information (referred to as the regularization term) is

$$R(a_i, l_i, a_{i-1}, l_{i-1}) = \alpha_a (a_i - a_{i-1})^2 + \alpha_l (l_i - l_{i-1})^2, \quad (3)$$

which restricts displacements $\{a_i, l_i\}$ of sample i to values close to the displacements $\{a_{i-1}, l_{i-1}\}$ of the previous sample $i - 1$. Symbols $\{\alpha_a, \alpha_l\}$ are axial and lateral regularization weights. For column j , the regularized cost function in DP is recursively formulated as

$$C_j^{(p)}(a_i, l_i, i) = [I_1(i, j) - I_2(i + a_i, j + l_i)]^2 + \min_{d_a, d_l} \left[\frac{C_j^{(p)}(d_a, d_l, i-1) + C_{j-1}^{(p)}(d_a, d_l, i)}{2} + R(a_i, l_i, d_a, d_l) \right] \quad (4)$$

where superscript p refers to the estimated pixel displacements (as opposed to subpixel/subsample estimates) and $\{d_a, d_l\}$ are the optimization parameters corresponding to axial and lateral displacements used to minimize the term within the bracket.

Likewise, terms a_i, l_i, d_a and d_l denote integer displacements. After calculating $C_j^{(p)}$, for $i = 2, \dots, m$, the cost function is minimized at $i = m$ with respect to integer values for a_m and l_m for all samples of the j^{th} line. Unlike [40], which calculates integer displacements for the entire image, we only utilize DP on a single line, referred to as the “seed” line. As described next, the integer displacement is refined to sub-pixel values.

B. DPAM: Dynamic Programming Analytic Minimization

Given the foregoing DP axial and lateral displacement estimates $\{a_i, l_i\}$, our goal is to find Δa_i and Δl_i such that $(a_i + \Delta a_i, l_i + \Delta l_i)$ are subsample values of axial and lateral displacements. We define a regularized cost function

$$C_j^{(s)}(\Delta a_1, \dots, \Delta a_m, \Delta l_1, \dots, \Delta l_m) = \sum_{i=1}^m \left\{ [I_1(i, j) - I_2(i + a_i + \Delta a_i, j + l_i + \Delta l_i)]^2 + \alpha (a_i + \Delta a_i - a_{i-1} - \Delta a_{i-1})^2 + \beta_a (l_i + \Delta l_i - l_{i-1} - \Delta l_{i-1})^2 + \beta'_l (l_i + \Delta l_i - l_{i, j-1})^2 \right\}, \quad (5)$$

where superscript s refers to subsample cost function and $\{\alpha, \beta_a, \beta'_l\}$ are regularization weights. To simplify the notation, we have dropped the index j in terms a_i and l_i in Eq. (5). In other words $a_i, l_i, \Delta a_i$ and Δl_i represent the displacements of sample (i, j) . Symbol $l_{i, j-1}$ is the lateral displacement of the previous RF-line. Note that $l_{i, j-1}$ denotes the total lateral displacement of the previous line, i.e., when the displacement of the $(j - 1)^{\text{th}}$ line was calculated, $l_{i, j-1}$ was updated with $l_{i, j-1} + \Delta l_{i, j-1}$. Eq. (5) is nonlinear because the variables Δa and Δl appear inside the nonlinear function I_2 . In addition, typical RF data contains around $m = 2000$ samples per line, leading to 4000 unknowns in Eq. (5) (taking into account the axial and lateral displacements for each sample). Consequently, the optimization of the cost function in Eq. (5) is intractable. In [44], we proposed to approximate

Algorithm 1 SESAME

```

1: procedure SESAME ( $A(i, j)$ ,  $L(i, j)$ )
2:   Pick a “seed” RF line for DP
3:    $a_i \leftarrow$  Integer axial Disp. using DP
4:    $l_i \leftarrow$  Integer lateral Disp. using DP
5:    $(a_i, l_i) \leftarrow$  Linear interpolation of the integer values
6:    $\Delta a_i$  &  $\Delta l_i \leftarrow$  SESAME with  $(a_i, l_i)$ 
7:    $a_i \leftarrow a_i + \Delta a_i$ ,  $l_i \leftarrow l_i + \Delta l_i$ 
8:   for <all RF lines>  $i$  do
9:      $a_{i+1} \leftarrow a_i$ ,  $l_{i+1} \leftarrow l_i$ 
10:     $\Delta a_{i+1}$  &  $\Delta l_{i+1} \leftarrow$  SESAME with  $(a_{i+1}, l_{i+1})$ 
11:     $a_{i+1} \leftarrow a_{i+1} + \Delta a_{i+1}$ ,  $l_{i+1} \leftarrow l_{i+1} + \Delta l_{i+1}$ 
12:  end for
13: end procedure

```

the summation term in Eq. (5) involving I_2 with the following first order Taylor series expansion

$$I_2(i + a_i + \Delta a_i, j + l_i + \Delta l_i) \approx I_2(i + a_i, j + l_i) + \Delta a_i I'_{2,a} + \Delta l_i I'_{2,l}, \quad (6)$$

where $I'_{2,a}$ and $I'_{2,l}$ are, respectively, the axial and lateral derivatives of I_2 . Substituting the above expression in Eq. (5) results in a quadratic equation, which can then be converted into a linear system of equations by setting its partial derivatives with respect to the optimization variables equal to zero. The linear system of equations has a sparse coefficient matrix, which can be exploited to solve the system in real time on a typical desktop computer [44].

C. SESAME: 2nd Order Analytical Minimization Elastography

The omission of higher order terms in the Taylor series expansion makes Eq. (6) less accurate, whereas inclusion of higher order terms renders the cost function intractable. In this section, we propose to include information from the second order derivative of the cost function while keeping the optimization problem tractable. The outline of our algorithm is presented in Algorithm 1.

The second order Taylor series expansion of term $I_2(i + a_i + \Delta a_i, j + l_i + \Delta l_i)$ in Eq. (5) contains Δa_i^2 and Δl_i^2 . Substituting these terms into Eq. (5) results in a polynomial cost function of order 4. Optimization of such a high dimensional 4th-order polynomial cost function is intractable. Instead of directly incorporating the second-order Taylor series term, we propose to penalize samples where this term is large and the first-order

Taylor expansion is not accurate. The revised cost function is

$$C_j^{(s)}(\Delta a_1, \dots, \Delta a_m, \Delta l_1, \dots, \Delta l_m) = \sum_{i=1}^m \left\{ w_{i,j} [I_1(i, j) - I_2(i + a_i + \Delta a_i, j + l_i + \Delta l_i)]^2 + \alpha (a_i + \Delta a_i - a_{i-1} - \Delta a_{i-1})^2 + \beta_a (l_i + \Delta l_i - l_{i-1} - \Delta l_{i-1})^2 + \beta_l (l_i + \Delta l_i - l_{i,j-1})^2 \right\}, \quad (7)$$

$$\text{where } w_{i,j} = \frac{1}{\epsilon + |I''_{2,a}(i, j)| + |I''_{2,l}(i, j)|}, \quad (8)$$

and ϵ a small positive constant to prevent the denominator from becoming zero. Symbols $|I''_{2,a}(i, j)|$ and $|I''_{2,l}(i, j)|$ denote the absolute values of the second-order derivatives of the intensities in the axial and lateral directions respectively. Intuitively speaking, incorporation of $w_{i,j}$ in the cost function penalizes samples that have a high curvature and, therefore, cannot be linearized.

If the displacement estimates associated with the previous line are inaccurate, they will affect the displacements of the next line through the last term in the right hand side of Eq. (7). We avoid propagating this error to the neighbouring RF lines by replacing β_l with

$$\beta_l^{(1)} = \frac{\beta_l}{1 + |r_{i,j-1}|}, \quad (9)$$

where $r_{i,j-1}$ is the residual associated with the displacement of sample i of the previous line. When there is a large residual, $\beta_l^{(1)}$ will be small and its influence on the next line is reduced.

The optimal $(\Delta a_i, \Delta l_i)$ values will make the partial derivatives of C_j with respect to Δa_i and Δl_i equal to zero. Setting $\partial C_j / \partial \Delta a_i = 0$ and $\partial C_j / \partial \Delta l_i = 0$, for $i = 1 \dots m$, and stacking the $2m$ unknowns in $\Delta d = [\Delta a_1, \Delta l_1, \Delta a_2, \Delta l_2, \dots, \Delta a_m, \Delta l_m]^T$ and $2m$ initial estimates in $d = [a_1, l_1, a_2, l_2, \dots, a_m, l_m]^T$ results in the matrix-vector representation

$$\underbrace{(\mathbf{I}_2^2 + \mathbf{D}_1 + \mathbf{D}_2)}_{\mathbf{A}} \Delta \mathbf{d} = \underbrace{\mathbf{I}'_2 \mathbf{e} - \mathbf{D}_1 \mathbf{d}}_{\mathbf{B}} \quad (10)$$

where $\mathbf{I}_2^2 = \text{diag}[\mathbf{J}'^2(1) \dots \mathbf{J}'^2(m)]$ is a symmetric tridiagonal matrix of size $(2m \times 2m)$ with

$$\mathbf{J}'^2(i) = \begin{bmatrix} I'_{2,a}{}^2 & I'_{2,a} I'_{2,l} \\ I'_{2,a} I'_{2,l} & I'_{2,l}{}^2 \end{bmatrix} \quad (11)$$

blocks on its diagonal entries where $I'_{2,a}$ and $I'_{2,l}$ are the derivatives of I_2 at point $(i + a_i, j + l_i)$ in the axial and lateral directions,

$$\mathbf{D}_1 = \begin{bmatrix} \alpha & 0 & -\alpha & 0 & 0 & 0 & \dots & 0 \\ 0 & \beta_\alpha & 0 & -\beta_\alpha & 0 & 0 & \dots & 0 \\ -\alpha & 0 & 2\alpha & 0 & -\alpha & 0 & \dots & 0 \\ 0 & -\beta_\alpha & 0 & 2\beta_\alpha & 0 & -\beta_\alpha & \dots & 0 \\ 0 & 0 & -\alpha & 0 & 2\alpha & 0 & \dots & 0 \\ \vdots & & & & & & \ddots & \\ 0 & 0 & 0 & \dots & -\alpha & 0 & \alpha & 0 \\ 0 & 0 & 0 & \dots & 0 & -\beta_\alpha & 0 & \beta_\alpha \end{bmatrix}, \quad (12)$$

and $\mathbf{D}_2 = \text{diag}(0, \beta'_1, 0, \beta'_1, \dots, 0, \beta'_1)$ is a diagonal matrix with dimensions $(2m \times 2m)$. Similarly, matrix \mathbf{I}'_2 is diagonal with the structure

$$\mathbf{I}'_2 = w_{i,j} \times \text{diag}(I'_{2,a}(1), I'_{2,l}(1), I'_{2,a}(2), I'_{2,l}(2), \dots, I'_{2,a}(m), I'_{2,l}(m)) \quad (13)$$

where $I'_{2,a}(i)$ and $I'_{2,l}(i)$ are calculated at site $(i+a_i, j+l_i)$ and $\mathbf{e} = [e_1 e_1 \dots e_m e_m]^T$ with $e_i = w_{i,j}(I_1(i, j) - I_2(i + a_i, j + l_i))$. Having $\Delta \mathbf{d} = [\Delta a_1, \Delta l_1, \Delta a_2, \Delta l_2, \dots, \Delta a_m, \Delta l_m]^T$ and $2m$ initial estimates in $\mathbf{d} = [a_1, l_1, a_2, l_2, \dots, a_m, l_m]$, we will find the $2m$ axial and lateral displacements for $i = 1 \dots m$ for line j . Afterwards, we follow the same procedure for the neighbouring line and consider the calculated displacement on line j as its initial value. Repeating this algorithm gives us both axial and lateral displacement values for the entire image.

On a related note, we observe Eq. (10) contains diagonal matrices ($\mathbf{D}_2, \Delta \mathbf{d}, \mathbf{I}'_2, \mathbf{d}$), tridiagonal matrix \mathbf{I}'_2 , and pentagonal matrix \mathbf{D}_1 . Using notations \mathbf{A} and \mathbf{B} in (10), the equation is formulated as $\mathbf{A} \Delta \mathbf{d} = \mathbf{B}$, which can be efficiently solved since \mathbf{A} is highly sparse. More specifically, Eq. (10) can be solved for \mathbf{d} in $9m$ operations since the coefficient matrix \mathbf{A} is pentadiagonal and symmetric. The number of computations is substantially less than $(2m)^3/3$, the number of operations required to solve a full linear system of simultaneous equations.

D. Numerical Simulations

Simulation data was used to assess the precision and accuracy of both DPAM and SESAME approaches. The probe specifications are listed in Table I. In order to model the tissue, a uniform phantom of dimension $(100 \times 50 \times 20)$ mm in axial, lateral and out-of-plane directions, respectively, with a constant attenuation coefficient of 0.45 dB/MHz/cm is considered. A minimum of 11 scatterers per resolution cell [34], [45] are uniformly distributed in the phantom with Gaussian scattering strengths [46]. Field II software [47] is used for the ultrasound simulation as is the case in [48]. The finite element ground truth displacement fields for shear wave propagation are provided by Quantitative Imaging Biomarkers Alliance (QIBA) [49], [50]. For each scatterer, the displacement is computed by interpolating the displacements of its neighbouring nodes using bilinear interpolation. The second image is generated after displacing all scatterers using Field II software. This procedure is repeated such that n total images are simulated during shear wave propagation. All simulations are repeated for point shear wave excitation at three different focal depths of 30, 50, and 70 mm, and for four different mediums having shear modulus of 1, 2, 5 and 10 KPa respectively. In addition, 25 independent speckle realizations were generated in all configurations using Field II.

E. Phantom Studies

A custom-made CIRS phantom (Norfolk, VA) with Young's modulus of 7KPa in the background including two lesions with different elasticities and material density of 1.03g/cm^3 is used in our studies. The lesions are placed far apart from each other

TABLE I
PARAMETERS FOR THE ARF SIMULATIONS.

Probe Parameters	Value
Center freq	3 MHz
Samp. freq	30 MHz
element height	14 mm
Element pitch	0.477 mm
Speed-of-sound	1540 m/s
Frac. bandwidth	100%
Elevation focus	50 mm
No. of elemets	128
Active elements	64



Fig. 2. Setup for phantom studies: The probe is hand-held during data collection from a CIRS elastography phantom. An excitation with period of $160\mu\text{s}$ at the focal depth of 20mm is applied as ARF and a set of 80 RF frames were acquired to monitor the shear-wave.

TABLE II
PARAMETERS FOR THE CUSTOM SHEAR-WAVE PHANTOM WITH LESION.

	Young's modulus (KPa)	Speed of Sound (m/s)
Background	7	1535
Lesion 1	21	1545
Lesion 2	45	1562

in the phantom. Therefore, the presence of a second lesion introduces little mutual interaction and has negligible impact on the first lesion. Young's modulus and speed of sound related to all the regions in the phantom are presented in Table II. In an isotropic medium, Young's modulus is approximately 3 times shear modulus. Thus in this paper we use shear modulus for comparison.

An Alpinion ECUBE R12 ultrasound machine (Bothell, WA) and an L3-8 transducer operating at frequency of 8MHz were used for data collection. The associated ARF parameters are listed in Table III. As shown in Fig. 2, the probe is hand-held during the data collection phase. Separate experiments are done on every region of the phantom (background, lesion 1, lesion 2) and results are compared using the proposed methods. Due to poor lateral resolution of ultrasound images (caused partly by the large pitch of the L3-8 transducer), up-sampling by a factor of 3 in the lateral direction is performed

TABLE III
PARAMETERS FOR THE REAL PHANTOM EXPERIMENTS.

Probe Parameters	Value
Excitation pulse length	160 μ s
Aperture size	64
Samp. freq. (f_c)	40 MHz
PRF	12 KHz
Element pitch	0.3 mm
Excitation focal depth	2 cm

for all methods. This is limited to experimental data, and no upsampling is performed for the simulated data. The SWS and shear modulus are related according to Eq. (2), which is used to estimate the shear modulus from SWS.

F. Validation Method

Normalized cross correlation (NCC) with a window-size of (70×10) samples and 98% kernel overlap with 2-dimensional parabolic interpolation of order 2 for estimation of subsample displacements was used for comparison. The selection of values of the NCC parameters, such as the window size, kernel overlap and interpolation method, are based on previously reported work [34], [38], [51]. A large kernel overlap generally improves the results but increases the computational complexity. We therefore used a large overlap to attain good results. A larger window-size usually reduces variance but increases the bias. We used larger windows than those reported in previous work to reduce the variance to the same order of magnitude as DPAM and SESAME. The displacement estimation results with a smaller NCC window-size is reported in the Supplementary Materials.

We calculate both axial and lateral displacements using NCC, DPAM or SESAME. The lateral displacement is only calculated to improve the quality of axial displacement estimates and is not used for calculating TOF. To calculate TOF and SWS, we follow the steps outlined in [26]. For quantitative comparison, the SNR is calculated using the following equations [52]

$$\text{SNR} = \frac{\mu^2}{\text{MSE}} \quad \text{and} \quad \text{MSE} = E[(d_e - \bar{d})^2], \quad (14)$$

where μ is the mean displacement value at a specific axial location on the excitation trajectory averaged over all the realizations, MSE denotes mean square error, and $\{d_e, \bar{d}\}$ are, respectively, the estimated and ground truth displacement fields. In experimental phantom study \bar{d} is unknown. Therefore, an average of 50 displacement estimates using NCC is used as the ground truth for \bar{d} . Results for each configuration included in the paper is based on 25 independent speckle realizations generated using Field II. For each configuration, we run the proposed methods and NCC on the 25 realizations. The statistical parameters, (e.g. mean, standard deviation, and their variations) are calculated based on the results of the 25 realizations for each configuration.

G. Execution Time

The NCC is implemented directly in MATLAB while the DPAM and SESAME algorithms are implemented in C++ as MATLAB Mex functions. An Intel i5-4690 3.50GHz CPU with 16GB of memory is used for signal processing. For the RF data of size (1388×150) , NCC, DPAM and SESAME take 42.4, 0.035 and 0.042 seconds, respectively. The NCC window-size is (70×10) samples and the overlap between successive windows is 98%. All reported execution times are calculated based on 150 independent executions of the programs in our Monte Carlo simulations.

III. RESULTS

A. Simulation Results

Fig. 3 shows the axial displacement field at 4ms following the excitation in the simulation phantom with the shear modulus of 10KPa and focal configuration of F/3.5. The phantom is excited at the focal point of 30mm. The FEM ground truth as well as the NCC, DPAM and SESAME displacement fields are shown. The colorbar is displayed in μ m and represents the common dynamic range used to plot the displacement frames. In Fig. 4, it is clear that both DPAM and SESAME outperform NCC in term of wavefront tracking which is quite significant for accurate SWS calculation.

Fig. 4 corresponds to axial displacement estimated from a uniform medium with a 10KPa shear modulus excited at the focal depth of 70mm. Displacement is plotted as a function of lateral direction calculated at the same depth as the excitation point in a range of 2-23mm for three different time instances of 1.5, 4, and 6.5ms following the excitation. Solid lines represent ground truth displacement, and the blue dotted, red and green dashed lines show displacement calculated using NCC, DPAM and SESAME methods, respectively. As observed, both DPAM and SESAME estimators outperform NCC in three aspects: 1) A displacement profile similar to the ground truth; 2) less underestimation (bias), and; (3) less jitter.

The SNR values associated with the displacements of the uniform phantom with the shear modulus of 10KPa at the ARF focal depths of 70mm are shown in Fig. 5 as a function of time. Error bars represent mean and standard deviation over 25 independent speckle realizations simulated using different random distribution of the scatterers. Results using the DPAM and SESAME estimators show the SNR improvement is achieved over the entire period of time. The error bars are large at the beginning ($t < 1$ ms) and at the end ($t > 3$ ms) of the plot in all cases. The reason is that tracking is difficult immediately following ARF due to initialization, and also a long time following the application of ARF due to attenuation of the shear waves.

Fig. 6 depicts time-step displacements for four independent materials with four different shear moduli of 1, 2, 5, 10KPa at a focal depth of 70mm and a lateral offset of 2.5mm from the excitation point. Higher shear modulus means that tissue is stiffer, which translates to a smaller displacement and consequently higher SWS which is what we expect. Comparison of the displacement profiles from (a) to (d) shows that, as expected, the shear wave propagates as μ is increased.

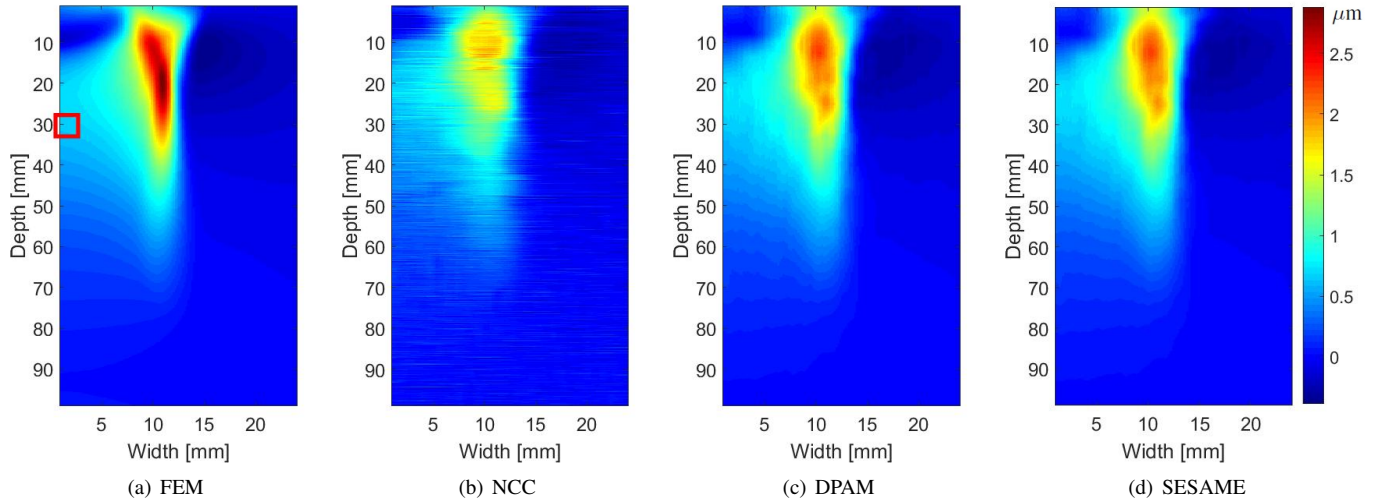


Fig. 3. Simulation results for a uniform medium with a shear modulus of 10KPa and F/3.5 focal configuration of 4ms following the excitation. Plot (a) shows the FEM (ground truth) axial displacement field while plots (b)-(d) are the corresponding displacement fields obtained from NCC, DPAM and SESAME, respectively. The focal excitation point is specified by a red square in plot (a) at a depth of 30mm. The common colorbar (shown on the extreme right hand side) for all plots is shown in μm and illustrates the dynamic range used to display the plots.

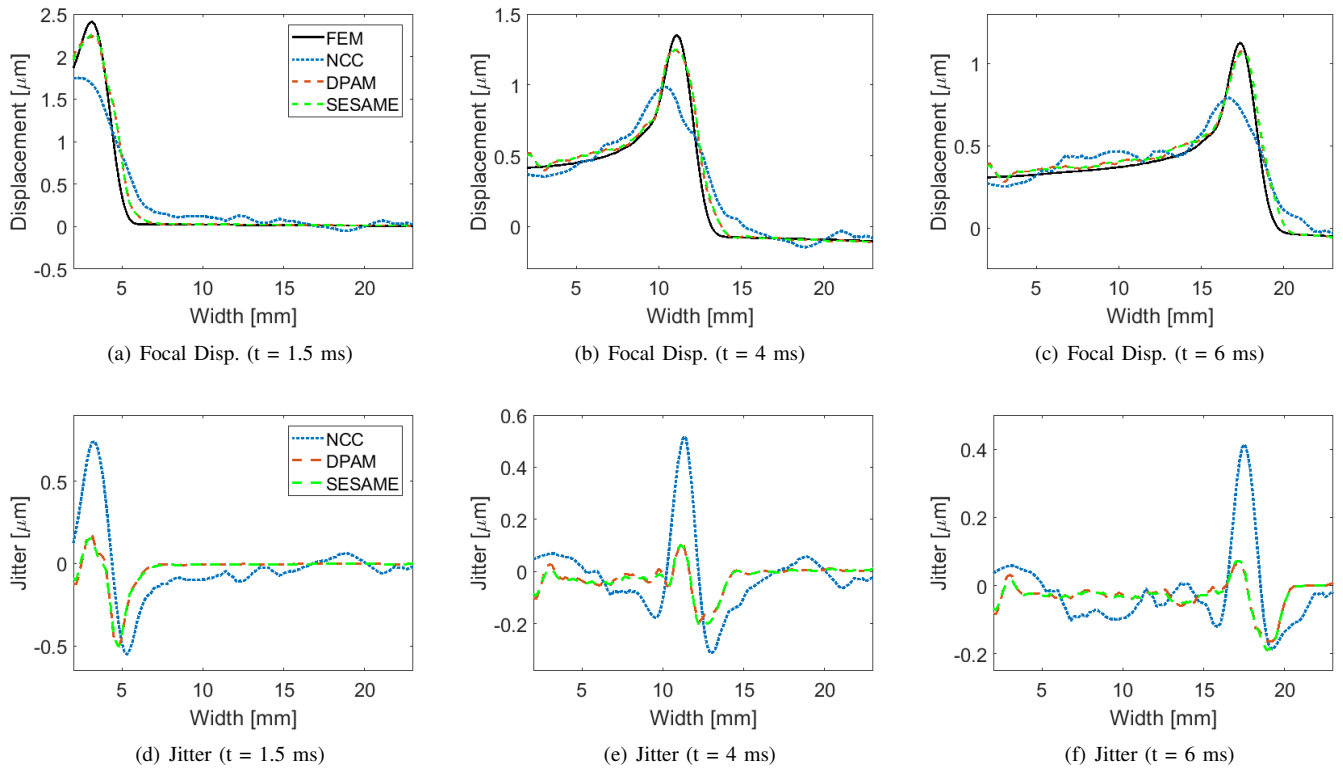


Fig. 4. Displacement field (first row) and jitter (second row) measured at a horizontal line located at the ARF depth at three different time instances following ARF.

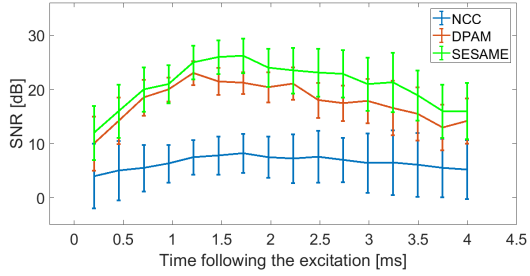


Fig. 5. Displacement SNR as a function of time following the excitation at the focal depth of 70 mm in a uniform simulation phantom with shear modulus of 10 KPa. Error bars show mean and variance over 25 independent realizations.

TABLE IV

PERFORMANCE OF THE PROPOSED METHODS AND NCC QUANTITATIVELY.

	NCC	DPAM	SESAME
SNR mean (dB)	7.5	20.4	24
%SNR variance	42	18	14
μ mean (KPa)	10.71	10.21	10.14
% μ variance	3.41	1.12	1.01
Execution time (s)	42.4	0.035	0.042

NCC suffers from a relatively large underestimation because it assumes constant displacement within the NCC window. In contrast, DPAM and SESAME estimate the displacement field for all samples of the RF data, and as such, the underestimation in displacement is substantially smaller.

In Fig. 7, the reconstructed shear moduli of the simulation phantom with 10KPa shear modulus is presented. The results are presented for point shear wave excitation at three focal depths of 30, 50, and 70mm. The TOF is estimated from the tracked displacement data [26], which yields SWS and subsequently the shear modulus (Eq. (2)). The results clearly demonstrate that both DPAM and SESAME substantially outperform NCC in both recovering the correct value of the shear modulus and producing a small estimation variance. The difference between reconstructed μ averaged over three different depths and true shear modulus are respectively 3.41%, 1.12%, and 1.01% of true μ for NCC, DPAM and SESAME. As the results of this figure corroborate, smaller shear modulus is estimated in deeper tissue, which is also observed in previous work [53].

Table IV quantitatively reports performance of the proposed methods and NCC using simulation data with shear modulus of 10KPa at depth 30mm. SNR value and its variation are calculated 2ms following the excitation using Eq. 14. Mean and variance of the estimated shear modulus are also reported in this table. All the variation are calculated over 25 independent realizations of the experiment. Execution times with the parameters mentioned in II-G are also reported. The difference in memory usage of DPAM and SESAME is negligible.

B. Experimental Phantom Results

Fig. 8 plots the signal-to-noise ratio (SNR) as a function of time following the ARF excitation focused at a depth

of 2cm. The experiment is repeated 25 times by randomly relocating the ultrasound probe. Blue, red and green curves correspond to the SNR values obtained from NCC, DPAM and SESAME, respectively. The error bars in Fig. 8 represent standard deviations over 25 experiments. Both DPAM and SESAME outperform NCC substantially and, on average, yield respective improvements of 7.6dB and 9.5dB in the displacement SNR. In addition, the results illustrate that approximately 7ms following the excitation, NCC SNR drops below 0dB while DPAM and SESAME maintain relatively high SNR values.

Fig. 9 shows reconstructed shear modulus μ of the phantom with a ground truth value for μ of 2.33KPa and material density of 1.03g/cm³. For the four depths of 18, 19.5, 21, and 22 mm, μ is calculated from SWS. The ground truth value is shown with a dashed line, and the results obtained from the NCC, DPAM and SESAME results are displayed in blue, red and green lines, respectively. The values of the bars from top to bottom respectively correspond to maximum, 75th percentile, median, 25th percentile and minimum measurements. Both DPAM and SESAME estimators yield a better performance in terms of both bias and variance. A comparison between DPAM and SESAME shows further improvements in estimating shear wave modulus and corresponding SNR in favour of DPAM in our experiments.

In the final experiment, we image a region of the phantom that contains a lesion to show the performance of the algorithm in more complex wave patterns. The CIRS phantom has two lesions with properties reported in Table II. ARF is applied at the depth of 30mm where both lesions are located. We repeat the imaging with focus at the same depth for 25 times by placing the probe at different locations over either of the two lesions. In Fig. 10, plot (a) represents reconstructed μ in lesion 1. Blue, red and green bars respectively represent reconstructed values using NCC, DPAM and SESAME. These methods are used for deformation tracking and TOF method is applied then to measure SWS and then μ . Horizontal black dashed-line shows the real value of the μ , which is provided by the manufacturer. Plot (b) is the same as plot (a) but the experiment is done on lesion 2 which contains a material with shear modulus of $\mu = 15$ KPa. The values of the bars from top to bottom respectively correspond to maximum, 75th percentile, median, 25th percentile and minimum measurements. Both DPAM and SESAME estimators yield a better performance in terms of both bias and variance. Furthermore, a comparison between DPAM and SESAME shows notable improvements in estimating shear modulus using SESAME over DPAM.

IV. DISCUSSIONS

On one hand, we incorporate prior information of displacement continuity into the cost function to prevent estimating physically unrealistic displacement fields and augment the RF data. On the other hand, we perform global minimization of the cost function to ensure that the optimization procedure is not trapped at a local minima. Our displacement estimation is, therefore, accurate and robust. In contrast to the window-based tracking methods [27], [29], no post-processing step is needed in the proposed approaches.

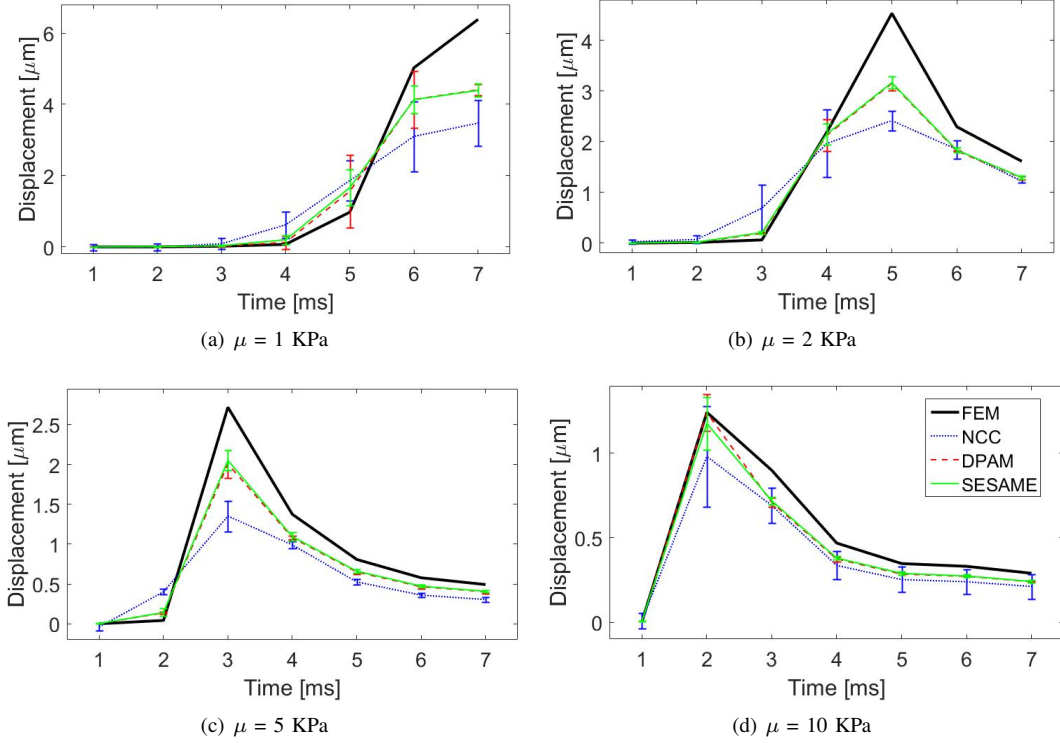


Fig. 6. Displacement profile in the simulation experiment at $z = \text{ARF}$ depth and 2.5 mm lateral offset from the ARF focus. Results for four simulation phantoms with different shear modulus (μ) of 1, 2, 5 and 10 KPa are shown. Error bars represent standard deviation of calculated displacements over 25 independent speckle realization. Greater μ relates to stiffer medium which yields faster wave propagation.

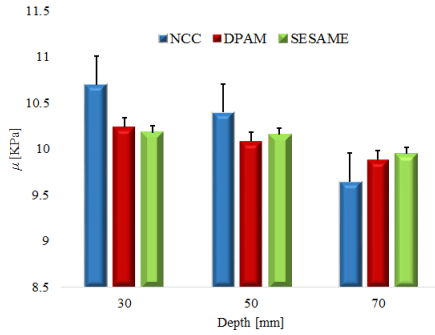


Fig. 7. Reconstructed shear moduli using displacement estimated using NCC (blue), DPAM (red) and SESAME (green) estimators for a uniform simulation phantom for excitation at three different focal points of 30, 50 and 70 mm. True shear modulus is 10 KPa. Bars and error bars respectively represent mean and variance over 25 independent realization.

In our experimental studies, the ground truth for displacement is unfortunately unknown. Therefore, it is common in the literature [38] to repeat the experiment for 25 times and use the mean of the results as the ground truth. Such an approach eliminates jitter in NCC estimates to a large extent but has little impact on the bias. See [34] for further discussion on the bias and variance of the NCC estimates. We have results from 50 experiments (instead of 25) to further reduce the variance of the estimated mean.

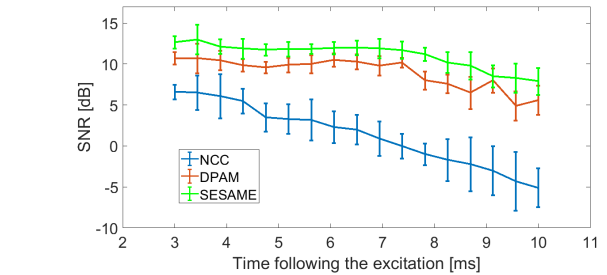


Fig. 8. Displacement SNR as a function of time following the excitation at the focal depth of 20 mm in the ROI in the background of the experimental phantom. Error bars show mean and variance over 25 data collections from the same phantom. NCC curve falls under 0 dB approximately after the wave travels for 7 ms due to the attenuation of the displacement amplitude.

The proposed DPAM and SESAME outperform NCC in two different aspects. First, the underestimation of the peak displacement field is much smaller because the displacements are estimated for each sample. In contrast, the window-based methods in essence calculate the average displacement within a window. Therefore, the estimate of the peak displacement is severely biased by the neighbouring samples that have lower displacements. As discussed in detail in [34], this issue is more important in SWE than in quasi-static elastography, since the displacement field is much more uniform in the latter. As verified experimentally, DPAM generates accurate

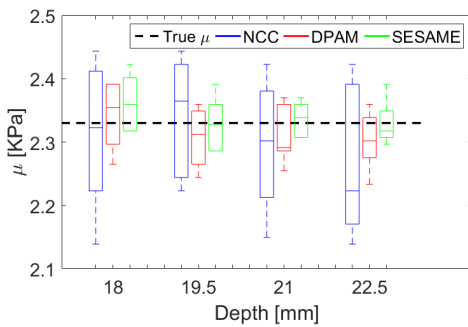


Fig. 9. Reconstructed shear moduli measured in ROI at four different depths. The excitation is at 20 mm depth. Tracking wavefront is done using NCC (blue), DPAM (red) and SESAME (green) in a tissue-mimicking phantom with given shear modulus of 2.33 KPa (black horizontal dashed line). Data collection is repeated 25 times at different locations of the phantom. From top to bottom, each bar shows maximum, 75%, median, 25% and maximum values.

displacement fields for quasi-static elastography and is more suitable for SWE. Second, less noisy displacement fields are generated with DPAM and SESAME with no need for post-processing to eliminate outliers or measurements with higher levels of noise.

We derive a nonlinear cost function with close to a million variables, which is intractable in its original form. We, therefore, linearize the derivative of the cost function to allow for efficient optimization. DPAM ignores second-order derivatives of the nonlinear terms, whereas SESAME takes into account the curvature of the nonlinear terms when linearizing the cost function. An important feature of SESAME is that the derivative of the cost function remains a linear and sparse system despite considering higher order derivatives. Therefore, SESAME outperforms DPAM with only a slightly higher computational complexity.

Both proposed methods are fast enough and suitable for real-time implementation. For instance, to find displacement field between two RF frames of size (1388×150) , the DPAM and SESAME estimators on average take 35 and 42ms, respectively, on a single core of a desktop CPU.

Figs. 3, 4, and 5 demonstrate accurate displacement estimation using DPAM and SESAME in a variety of simulations with acoustic radiation force focusing on different excitation regions. In comparison with NCC, the proposed estimators track displacements more accurately such that smaller jitter and higher SNR are obtained. Fig. 6 illustrates that NCC, DPAM and SESAME predict faster SWS in a medium with higher elasticity.

The results of Fig. 7 demonstrate less variability and more accurate μ estimation using the proposed methods compared to NCC. The dependency of shear modulus estimation on excitation focal depth is also described in [53]. Overall, the estimated values of μ averaged over three examined depths are 10.34, 10.11, and 10.10KPa using NCC, DPAM and SESAME for a phantom with a ground truth value of $\mu = 10$ KPa.

Regions with large values of the second order derivative are high in texture and can aid tracking. However, there are two reasons that we penalize these regions. First, cost function

of DPAM makes the assumption that RF data around each sample is linear. Regions with a high second-order derivative render this assumption inaccurate. In other words, Eq. 5 is not a good approximation for Eq. 4, and therefore, its optimum value is not an optimum value of Eq. 4. Selecting linear regions of the image that are suitable for the optimization technique has been shown to improve tracking results in the field of computer vision [54]. Second, penalizing regions with high second-order derivative does not deprive SESAME from suitable regions for tracking. SESAME utilizes regions of the RF data that have high derivative values (positive or negative). Since SESAME considers the entire RF data set for the purpose of optimizations, these regions with negative and positive derivatives provide SESAME with texture needed for tracking accurately.

The large improvement in displacement estimation in DPAM and SESAME is a result of the spatial regularization in the cost function, which strikes a balance between data and smoothness terms. We expect that regularization in the temporal domain, which considers the equations of wave motion, to further improve the results. Moreover, temporal regularization can distinguish motions caused by wave propagation from physiological motions since the physics that governs these motions are different. This is an interesting avenue for future work.

V. CONCLUSION

We proposed two methods, DPAM and SESAME, for estimating sub-pixel tissue displacements in shear wave elastography. The associated cost function used to estimate the axial and lateral displacement fields is non-linear and has high-dimensions with close to a million variables. We simplified both approaches into linear systems of equations with sparse matrix-vector representations that can be solved in real time in a few milliseconds on a typical desktop computer. DPAM approximates the nonlinear terms using a first order Taylor series expansion, whereas SESAME takes into account second-order derivatives of the nonlinear terms. DPAM and SESAME have similar computational complexity though SESAME outperforms DPAM in terms of estimation bias and variance. Both approaches are suitable for real-time implementation on commercial ultrasound machines and will hopefully lead to more robust SWE for clinical adoption.

ACKNOWLEDGMENT

The authors would like to thank Julian Lee from Alpinion Ultrasound for technical support and for loaning the L3-8 transducer as well as Mark Palmeri for providing the shear wave simulation data. The work presented in this paper is supported by NSERC Discovery Grants RGPIN-2017-06629 and RGPIN-2015-04136.

REFERENCES

- [1] A. P. Sarvazyan, O. V. Rudenko, S. D. Swanson, J. B. Fowlkes, and S. Y. Emelianov, "Shear wave elasticity imaging: a new ultrasonic technology of medical diagnostics," *Ultrasound in medicine & biology*, vol. 24, no. 9, pp. 1419–1435, 1998.

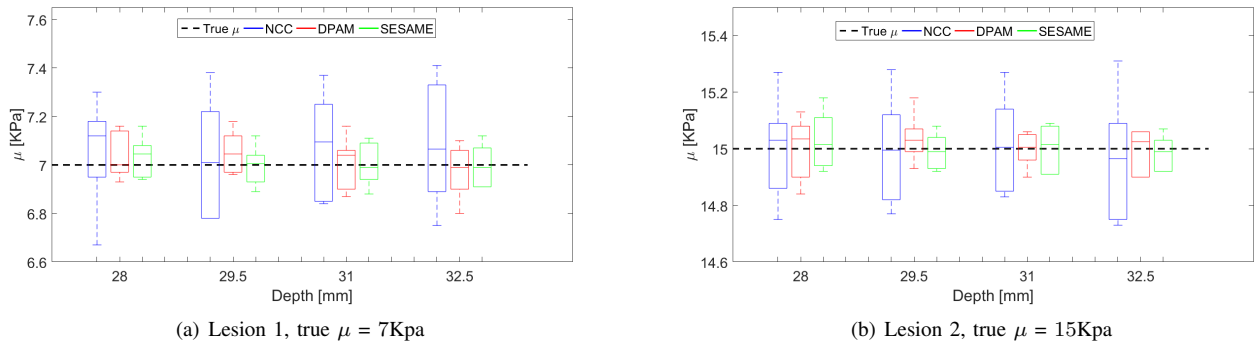


Fig. 10. Plots (a) and (b) represent reconstructed shear moduli measured in ROI at four different depths inside the lesion 1 and lesion 2, respectively. The excitation is at 30 mm depth where both lesions are located. Tracking wavefront is done using NCC (blue), DPAM (red) and SESAME (green) in a tissue-mimicking phantom with given shear modulus of 7KPa and 15KPa (black horizontal dashed lines) for lesion 1 and lesion 2, respectively. Data collection is repeated 25 times for each lesion. From top to bottom, each bar shows maximum, 75%, median, 25% and minimum values.

- [2] J. Ophir, B. Garra, F. Kallel, E. Konofagou, T. Krouskop, R. Righetti, and T. Varghese, "Elastographic imaging," *Ultrasound in medicine & biology*, vol. 26, pp. S23–S29, 2000.
- [3] L. Sandrin, M. Tanter, S. Catheline, and M. Fink, "Shear modulus imaging with 2-d transient elastography," *IEEE transactions on ultrasonics, ferroelectrics, and frequency control*, vol. 49, no. 4, pp. 426–435, 2002.
- [4] S. Catheline, F. Wu, and M. Fink, "A solution to diffraction biases in sonoelasticity: the acoustic impulse technique," *J. Acoust. Soc. Amer.*, vol. 105, no. 5, pp. 2941–2950, 1999.
- [5] K. Nightingale, S. McAleavey, and G. Trahey, "Shear-wave generation using acoustic radiation force: in vivo and ex vivo results," *Ultrasound in medicine & biology*, vol. 29, no. 12, pp. 1715–1723, 2003.
- [6] J. Bamber *et al.*, "Efsmb guidelines and recommendations on the clinical use of ultrasound elastography. part 1: Basic principles and technology," *Ultraschall in der Medizin-European Journal of Ultrasound*, vol. 34, no. 02, pp. 169–184, 2013.
- [7] C. Sumi, "Reconstructions of shear modulus, poisson's ratio, and density using approximate mean normal stress," *IEEE TUFFC*, vol. 53, 2006.
- [8] C. Pellot-Barakat, F. Frouin, M. F. Insana, and A. Herment, "Ultrasound elastography based on multiscale estimations of regularized displacement fields," *IEEE TMI*, vol. 23, no. 2, pp. 153–163, 2004.
- [9] J. Bercoff, M. Tanter, S. Chaffai, and M. Fink, "Ultrafast imaging of beamformed shear waves induced by the acoustic radiation force. application to transient elastography," in *Proceedings of the 2002 IEEE Ultrasonics Symposium*, vol. 2, 2002, pp. 1899–1902.
- [10] J.-L. Gennisson, T. Deffieux, M. Fink, and M. Tanter, "Ultrasound elastography: principles and techniques," *Diagnostic and interventional imaging*, vol. 94, no. 5, pp. 487–495, 2013.
- [11] K. Nightingale, "Acoustic radiation force impulse (arfi) imaging: a review," *Current med imag reviews*, vol. 7, no. 4, pp. 328–339, 2011.
- [12] K. R. Nightingale, M. L. Palmeri, R. W. Nightingale, and G. E. Trahey, "On the feasibility of remote palpation using acoustic radiation force," *J. Acoust. Soc. Amer.*, vol. 110, no. 1, pp. 625–634, 2001.
- [13] C. Sumi, "Usefulness of ultrasonic strain measurement-based shear modulus reconstruction for diagnosis and thermal treatment," *IEEE TUFFC*, vol. 52, no. 10, pp. 1670–1689, Oct. 2005.
- [14] J. R. Doherty, G. E. Trahey, K. R. Nightingale, and M. L. Palmeri, "Acoustic radiation force elasticity imaging in diagnostic ultrasound," *IEEE transactions on ultrasonics, ferroelectrics, and frequency control*, vol. 60, no. 4, pp. 685–701, 2013.
- [15] J. Bercoff, M. Tanter, and M. Fink, "Supersonic shear imaging: a new technique for soft tissue elasticity mapping," *IEEE TUFFC*, vol. 51, no. 4, pp. 396–409, 2004.
- [16] M. Fink and M. Tanter, "A multiwave imaging approach for elastography," *Curr Med Imag Rev*, vol. 7, no. 4, pp. 340–349, 2011.
- [17] C. A. Carrascal, S. Chen, A. Manduca, J. F. Greenleaf, and M. Urban, "Improved shear wave group velocity estimation method based on spatiotemporal peak and thresholding motion search," *IEEE Transactions on Ultrasonics, Ferroelectrics, and Frequency Control*, 2017.
- [18] S. Y. Lee, A. R. Cardones, J. Doherty, K. Nightingale, and M. Palmeri, "Preliminary results on the feasibility of using arfi/swei to assess cutaneous sclerotic diseases," *Ultrasound in medicine & biology*, vol. 41, no. 11, pp. 2806–2819, 2015.
- [19] R. Sinkus, M. Tanter, T. Xydeas, S. Catheline, J. Bercoff, and M. Fink, "Viscoelastic shear properties of in vivo breast lesions measured by mr elastography," *Mag res imaging*, vol. 23, no. 2, pp. 159–165, 2005.
- [20] T. E. Oliphant, A. Manduca, R. L. Ehman, and J. F. Greenleaf, "Complex-valued stiffness reconstruction for magnetic resonance elastography by algebraic inversion of the differential equation," *Magnetic resonance in Medicine*, vol. 45, no. 2, pp. 299–310, 2001.
- [21] E. E. Van Houten, M. M. Doyley, F. E. Kennedy, J. B. Weaver, and K. D. Paulsen, "Initial in vivo experience with steady-state subzone-based mr elastography of the human breast," *Journal of magnetic resonance imaging*, vol. 17, no. 1, pp. 72–85, 2003.
- [22] M. Honarvar, R. Sahebjavaher, R. Rohling, and S. Salcudean, "A comparison of fem-based inversion algorithms, local frequency estimation and direct inversion approach used in mr elastography," *IEEE Transactions on Medical Imaging*, 2017.
- [23] M. Honarvar, R. Rohling, and S. Salcudean, "A comparison of direct and iterative finite element inversion techniques in dynamic elastography," *Physics in medicine and biology*, vol. 61, no. 8, p. 3026, 2016.
- [24] M. Tanter, J. Bercoff, A. Athanasiou, T. Deffieux, J.-L. Gennisson, G. Montaldo, M. Muller, A. Tardivon, and M. Fink, "Quantitative assessment of breast lesion viscoelasticity: initial clinical results using supersonic shear imaging," *Ultrasound in medicine & biology*, vol. 34, no. 9, pp. 1373–1386, 2008.
- [25] J. McLaughlin and D. Renzi, "Shear wave speed recovery in transient elastography and supersonic imaging using propagating fronts," *Inverse Problems*, vol. 22, no. 2, p. 681, 2006.
- [26] M. L. Palmeri, M. H. Wang, J. J. Dahl, K. D. Frinkley, and K. R. Nightingale, "Quantifying hepatic shear modulus in vivo using acoustic radiation force," *UMB*, vol. 34, no. 4, pp. 546–558, 2008.
- [27] M. H. Wang, M. L. Palmeri, V. M. Rotemberg, N. C. Rouze, and K. R. Nightingale, "Improving the robustness of time-of-flight based shear wave speed reconstruction methods using ransac in human liver in vivo," *Ultrasound in medicine & biology*, vol. 36, no. 5, pp. 802–813, 2010.
- [28] J. McLaughlin and D. Renzi, "Using level set based inversion of arrival times to recover shear wave speed in transient elastography and supersonic imaging," *Inverse Problems*, vol. 22, no. 2, p. 707, 2006.
- [29] N. C. Rouze, M. H. Wang, M. L. Palmeri, and K. R. Nightingale, "Robust estimation of time-of-flight shear wave speed using a radon sum transformation," *IEEE transactions on ultrasonics, ferroelectrics, and frequency control*, vol. 57, no. 12, pp. 2662–2670, 2010.
- [30] L. Guo, Y. Xu, Z. Xu, and J. Jiang, "A pde-based regularization algorithm toward reducing speckle tracking noise: A feasibility study for ultrasound breast elastography," *Ultrasonic imaging*, vol. 37, no. 4, pp. 277–293, 2015.
- [31] C. Pellot-Barakat, M. Lefort, L. Chami, M. Labit, F. Frouin, and O. Lucidarme, "Automatic assessment of shear wave elastography quality and measurement reliability in the liver," *Ultrasound in medicine & biology*, vol. 41, no. 4, pp. 936–943, 2015.
- [32] M. Friedrich-Rust, K. Wunder, S. Kriener, F. Sotoudeh, S. Richter,

- J. Bojunga, E. Herrmann, T. Poynard, C. F. Dietrich, J. Vermehren *et al.*, "Liver fibrosis in viral hepatitis: noninvasive assessment with acoustic radiation force impulse imaging versus transient elastography 1," *Radiology*, vol. 252, no. 2, pp. 595–604, 2009.
- [33] W. F. Walker and G. E. Trahey, "A fundamental limit on the performance of correlation based phase correction and flow estimation techniques," *IEEE Transactions on Ultrasonics, Ferroelectrics, and Frequency Control*, vol. 41, no. 5, pp. 644–654, 1994.
- [34] M. L. Palmeri, S. A. McAleavey, G. E. Trahey, and K. R. Nightingale, "Ultrasonic tracking of acoustic radiation force-induced displacements in homogeneous media," *IEEE transactions on ultrasonics, ferroelectrics, and frequency control*, vol. 53, no. 7, pp. 1300–1313, 2006.
- [35] M. McCormick, N. Rubert, and T. Varghese, "Bayesian regularization applied to ultrasound strain imaging," *IEEE Transactions on Biomedical Engineering*, vol. 58, no. 6, pp. 1612–1620, 2011.
- [36] B. C. Byram, G. E. Trahey, and M. L. Palmeri, "Effect of prior probability quality on biased time-delay estimation," *Ultrasonic imaging*, vol. 34, no. 2, pp. 65–80, 2012.
- [37] B. Byram, G. E. Trahey, and M. Palmeri, "Bayesian speckle tracking. part ii: biased ultrasound displacement estimation," *IEEE trans ultrasonics, ferroelectrics frequency control*, vol. 60, no. 1, pp. 144–157, 2013.
- [38] D. M. Dumont and B. C. Byram, "Robust tracking of small displacements with a bayesian estimator," *IEEE transactions on ultrasonics, ferroelectrics, and frequency control*, vol. 63, no. 1, pp. 20–34, 2016.
- [39] H. Rivaz, E. M. Boctor, M. A. Choti, and G. D. Hager, "Real-time regularized ultrasound elastography," *IEEE transactions on medical imaging*, vol. 30, no. 4, pp. 928–945, 2011.
- [40] H. Rivaz, E. Boctor, P. Foroughi, R. Zellars, G. Fichtinger, and G. Hager, "Ultrasound elastography: a dynamic programming approach," *Medical Imaging, IEEE Transactions on*, vol. 27, no. 10, pp. 1373–1377, 2008.
- [41] H. Rivaz, "Incorporating second-order derivatives into real-time regularized ultrasound elastography," *Int. Tissue Elasticity Conf. ITEC*, 2015.
- [42] M. D. Horeh, A. Asif, and H. Rivaz, "Regularized tracking of shear-wave in ultrasound elastography," *The 42nd IEEE Int. Conference on Acoustic, Speech and Signal Processing (ICASSP), New Orleans, LA, 2017*, p. In press, 2017.
- [43] R. E. Bellman and S. E. Dreyfus, *Applied dynamic programming*. Princeton university press, 2015.
- [44] H. Rivaz, E. M. Boctor, M. A. Choti, and G. D. Hager, "Ultrasound elastography using multiple images," *Medical image analysis*, vol. 18, no. 2, pp. 314–329, 2014.
- [45] H. Rivaz, E. M. Boctor, and G. Fichtinger, "P3e-9 ultrasound speckle detection using low order moments," in *2006 IEEE Ultrasonics Symposium*. IEEE, 2006, pp. 2092–2095.
- [46] R. F. Wagner, S. W. Smith, J. M. Sandrik, and H. Lopez, "Statistics of speckle in ultrasound b-scans," *IEEE Transactions on sonics and ultrasonics*, vol. 30, no. 3, pp. 156–163, 1983.
- [47] J. A. Jensen, "Field: A program for simulating ultrasound systems," in *10TH Nordic Conference on Biomedical Imaging, VOL. 4, supplement 1, PART 1: 351–353*. Citeseer, 1996.
- [48] M. L. Palmeri, A. C. Sharma, R. R. Bouchard, R. W. Nightingale, and K. R. Nightingale, "A finite-element method model of soft tissue response to impulsive acoustic radiation force," *IEEE Trans ultrasonics, ferroelectrics, frequency control*, vol. 52, no. 10, pp. 1699–1712, 2005.
- [49] M. Palmeri and B. Qiang, "Rsna-qiba-us-sws/qiba-digitalphantoms v1.0.0," Oct. 2016.
- [50] M. L. Palmeri, B. Qiang, S. Chen, and M. W. Urban, "Guidelines for finite-element modeling of acoustic radiation force-induced shear wave propagation in tissue-mimicking media," *IEEE TUFFC*, vol. 64, no. 1, pp. 78–92, 2017.
- [51] D. M. Giannantonio, D. M. Dumont, G. E. Trahey, and B. C. Byram, "Comparison of physiological motion filters for in vivo cardiac arfi," *Ultrasonic imaging*, vol. 33, no. 2, pp. 89–108, 2011.
- [52] D. M. Dumont, K. M. Walsh, and B. C. Byram, "Improving displacement signal-to-noise ratio for low-signal radiation force elasticity imaging using bayesian techniques," *Ultrasound in medicine & biology*, 2016.
- [53] Y. Wang, B. Peng, and J. Jiang, "Building an open-source simulation platform of acoustic radiation force-based breast elastography," *Physics in Medicine and Biology*, vol. 62, no. 5, p. 1949, 2017.
- [54] S. Benhimane, A. Ladikos, V. Lepetit, and N. Navab, "Linear and quadratic subsets for template-based tracking," in *IEEE Conference Computer Vision and Pattern Recognition*. IEEE, 2007, pp. 1–6.